Structural and thermodynamic characterization of CuZr metallic glass nanoparticles: Insights from atomistic simulations

Xuezhen Ren [1], Suyue Yuan [1,2] Emily J. Gurniak [1], and Paulo S. Branicio [1,*]

[1]*Mork Family Department of Chemical Engineering and Materials Science, University of Southern California, 3651 Watt Way, VHE 602, Los Angeles, California 90089-0242, USA*

[2]*Materials Science Division, Lawrence Livermore National Laboratory, Livermore, California 94550, USA*

(Received 17 November 2023; accepted 8 March 2024; published 10 April 2024)

Metallic crystalline nanoparticles (NPs) have been shown to display intriguing size-dependent properties. However, the properties of metallic glass (MG) NPs remain largely unexplored. Using molecular dynamics simulations, we produce $Cu_{64}Zr_{36}$ MG NPs ranging in size from 1 to 20 nm by cooling molten systems at a relatively slow rate of 10^9 K/s. Results indicate that NPs are coated with a Cu-rich layer with a thickness that increases with NP size. We employ various simulated rates of heating, from 10^{11} to 10^{13} K/s, to determine the melting points of these NPs. The results show a significant decrease in the solidus temperature for NPs smaller than 10 nm. Furthermore, as NP size decreases, the fraction of Cu full icosahedra within the NPs increases, suggesting that smaller NPs are stronger and harder. These findings provide insights for designing heterogeneous metallic nanoglass materials that leverage the size-dependent properties of MG NPs.

DOI: 10.1103/PhysRevMaterials.8.046001

I. INTRODUCTION

The lack of long-range structural order, characteristic of metallic glasses (MGs), can be achieved by rapid quenching from a molten state. The distinctive structure provides MGs with remarkable properties. Particularly, MGs demonstrate enhanced strength, notable electrical conductivity, and a spectrum of engineering attributes, positioning them as valuable materials in mechanical, electrical, and biomedical applications [1,2]. Over the last few decades, prototypes using MGs have shown properties unmatched by established materials [3–7]. In particular, glassy nanoparticles (NPs) have garnered significant attention [8–16]. By combining nanoscale features and amorphous structures, glassy NPs display vast potential bolstered by advancing nanotechnology techniques.

Relative to nanocrystalline alloys [9], ceramic NPs, and organic NPs, the properties of glassy NPs remain underexplored. The prevailing knowledge of glassy NPs is based on a limited number of studies investigating their uses, such as in nanoglasses [16–18]. In molecular dynamics (MD) simulations, glassy NPs are prepared through either inert gas condensation (IGC) or melting and quenching spherical sections derived from bulk MG samples. Adajaoud *et al.* [18] have previously shown that NPs generated from the two methods are similar while the latter approach allows for better NP size control. A consistent characteristic of glassy NPs is the surface segregation effect, observed both experimentally and through computational means. In the case of CuZr NPs, the lighter Cu atoms tend to migrate to the surface, resulting in a Cu-rich shell that envelops a rather uniform core region. This surface structure is pivotal for the properties of glass-glass interfaces in nanoglasses that are generated through the condensation of these glassy NPs. However, the structural development of CuZr MG NPs during synthesis, characterized by the emergence of short-to-medium range order, along with their thermal stability and size-dependent characteristics, remains to be comprehensively explored.

In this study, we conduct a detailed examination of the microscopic characteristics of CuZr glassy NPs by presenting a comprehensive set of NPs with diameters spanning 1–20 nm. These NPs are generated employing quenching simulations using a rate of 10^9 K/s, which is notably slower by an order of magnitude compared to typical rates in MD simulations. We observe notable size-dependent properties of $Cu_{64}Zr_{36}$ MG NPs in the 4–20-nm range, as evidenced by Cu composition, Voronoi polyhedron analysis, melting behavior, and glass transition temperatures. Our observations are consistent with previous NP studies, enhance our understanding of MG NPs, and offer crucial insights for NP selection in nanoglass synthesis.

II. METHODOLOGY

All MD simulations are performed with LAMMPS [19]. The atomic interactions in this study are calculated based on the embedded atom model (EAM) potential for Cu-Zr alloys developed by Mendelev *et al.* [20]. Throughout the simulations, we employ a constant integration time step of 2 fs. To prepare the nanoparticles (NPs), we start with a periodic bulk crystalline sample with 16 000 atoms arranged in a face-centered-cubic (fcc) lattice structure. To enforce the desired chemical composition, 36% of atoms are randomly assigned as Zr and the remaining as Cu. This bulk sample undergoes a heating step from 50 to 1800 K at a rate of 10^{11} K/s, which is followed by a cooling step back to 50 K

*branicio@usc.edu

TABLE I. Size, composition, and surface energy of CuZr nanoparticles (NPs).

Diameter (nm)	Total number of atoms	Fraction of Cu atoms	Surface Energy (J/m^2)
1	50	0.640	1.28
2	256	0.641	1.16
3	895	0.640	1.18
4	2,073	0.638	1.09
5	4,075	0.639	1.12
6	7,027	0.642	1.17
7	11,170	0.642	1.19
8	16,677	0.641	1.16
9	23,715	0.640	1.14
10	32,516	0.641	1.15
11	43,283	0.640	1.14
12	56,214	0.641	1.14
13	71,485	0.640	1.15
14	89,223	0.641	1.17
15	109,777	0.641	1.16
16	133,204	0.641	1.18
17	159,777	0.641	1.16
18	189,648	0.641	1.17
19	223,051	0.641	1.19
20	260,200	0.641	1.20

at a rate of 10^9 K/s under constant 0 Pa pressure. This process results in a well-relaxed, homogeneously composed MG configuration. Subsequent to this, we extract spherical-shaped NPs of varying sizes from this bulk MG sample after replicating it to the desired dimensions; e.g., for the production of 3–10-nm NPs, the original MG system undergoes a $2 \times 2 \times 2$ replication, while a $3 \times 3 \times 3$ replication is used for 11–17-nm NPs, and a $4 \times 4 \times 4$ replication is required to carve out 18–20-nm NPs. A detailed breakdown of system size and Cu atom fractions, indicative of the composition of each NP, is presented in Table I. For the next phase, we simulated the melting process on the generated NPs by raising their temperature from 50 to 1800 K at a rate of 10^{11} K/s. These molten CuZr clusters are then thermalized at 1800 K for 10 ns. Following this thermalization, we quench the molten CuZr cluster from 1800 K down to 50 K at 10^9 K/s, in a long, 1.75-μs, simulation run. After two rounds of melt-and-quench procedures, the resulting NPs achieve a deeply relaxed MG structure.

To evaluate the melting points of the NPs, we utilize three distinct heating rates in the simulations: 10^{13}, 10^{12}, and 10^{11} K/s. We increment the temperature in steps of 50 K, from 50 to 1800 K. The chosen heating rate dictates the duration for which the NPs are maintained at every temperature level. Specifically, durations of 2500, 25 000, and 250 000 time steps correspond to the rates of 10^{13}, 10^{12}, and 10^{11} K/s, respectively. The schematic of the NP generation procedure is represented in Fig. 1. We carry out atomic Voronoi analyses on the relaxed NPs to identify Cu-centered full icosahedral (FI), which have a Voronoi index of ⟨0,0,12,0⟩. For visualization and data analysis, we utilized the OVITO package [21]. To accelerate the MD simulations, we leverage the GPU implementation of the EAM potential in LAMMPS, performing all calculations using a combination of CPUs and GPUs. Among all the simulations, the most resource intensive is the one devised for the 20-nm NP. This simulation, when executed using 160 Xeon-2640v4 CPU cores combined with 16 NVIDIA Tesla P100 GPUs, demands approximately 605 h of computational wall-clock time.

III. RESULTS

During quenching, the potential energy of the NP diminishes as temperature drops, as demonstrated in Fig. S1 of the Supplemental Material [22] for 4–6-nm NPs. At the glass transition temperature (T_g), there is an alteration in the NP thermal properties, which causes a distinct shift in the slope of the potential energy versus temperature curves. By interpolating the slopes on both sides of this inflection point, the intersection temperature is identified as the NP T_g. Figure 2 shows T_g values for 4–20-nm NPs plotted against their respective diameters. The T_g consistently increases with NP size. Notably, the increment in T_g is more pronounced for smaller NPs (4–10 nm), whereas it tends to converge at sizes above 20 nm. Drawing parallels with the thermal behavior in crystalline NPs [23], the temperature-diameter relationship is modeled using the T_g of the bulk MG and the surface-to-volume ratio of the NPs, represented as $6/d$, where d is the NP diameter. Using this model, the relationship takes the form $T_g = T_{g(\text{bulk})} - a \times (\frac{6}{d})^n$. Using $T_{g(\text{bulk})} = 692$ K, the fitting parameters are found to be $a = 68.8$ and $n = 1.3$. The fitted curve is shown as a dashed line in Fig. 2 and indicates an excellent agreement with the calculated values of T_g.

To investigate the structure of NPs, the atomic coordinates for 4–20-nm NPs are interpreted through visualization and data analysis. An initial probe into the compositional analysis reveals a radial transition in the NPs with significant Cu segregation to their surface. By measuring the distance from the center of mass to the surface, atoms are segmented into spherical subshells 0.02 nm thick, and the average fraction of Cu in each subshell is determined. Figure 3 shows this fraction plotted against the distance of the subshell to the surface displaying a region at the surface with high concentration in Cu with a width exceeding 0.2 nm. This surface segregation effect agrees with previously identified characteristics of MG NPs formed either by IGC or melt quenching of NPs from bulk MG [8,10,13,18]. Beyond the immediate surface region, the Cu fraction quickly falls below 0.64, which is the overall fraction of Cu in the NPs, before stabilizing near 0.64 towards the core of the NP. This analysis also compares the compositional trends of NPs of different sizes, demonstrating that the thickness of the Cu-rich layer slightly expands with increasing NP size. While the thickness of the Cu-rich layer for the 6-nm NP is 0.27 nm, the thickness for the 20-nm NP reaches 0.42 nm.

While surface segregation is a well-reported phenomenon in MG nanoparticles, it is worthwhile to also analyze composition fluctuations at the core of the particles. In Fig. 4, we shift our focus to the center of the NPs. The fraction of Cu in the core is evaluated in 0.5-nm-thick shells around the center of mass up to a radius of 2.5 nm, for 6–20-nm NPs. A thicker shell is used here compared to that used in Fig. 3 to reduce statistical fluctuations, since from the center of mass the shells

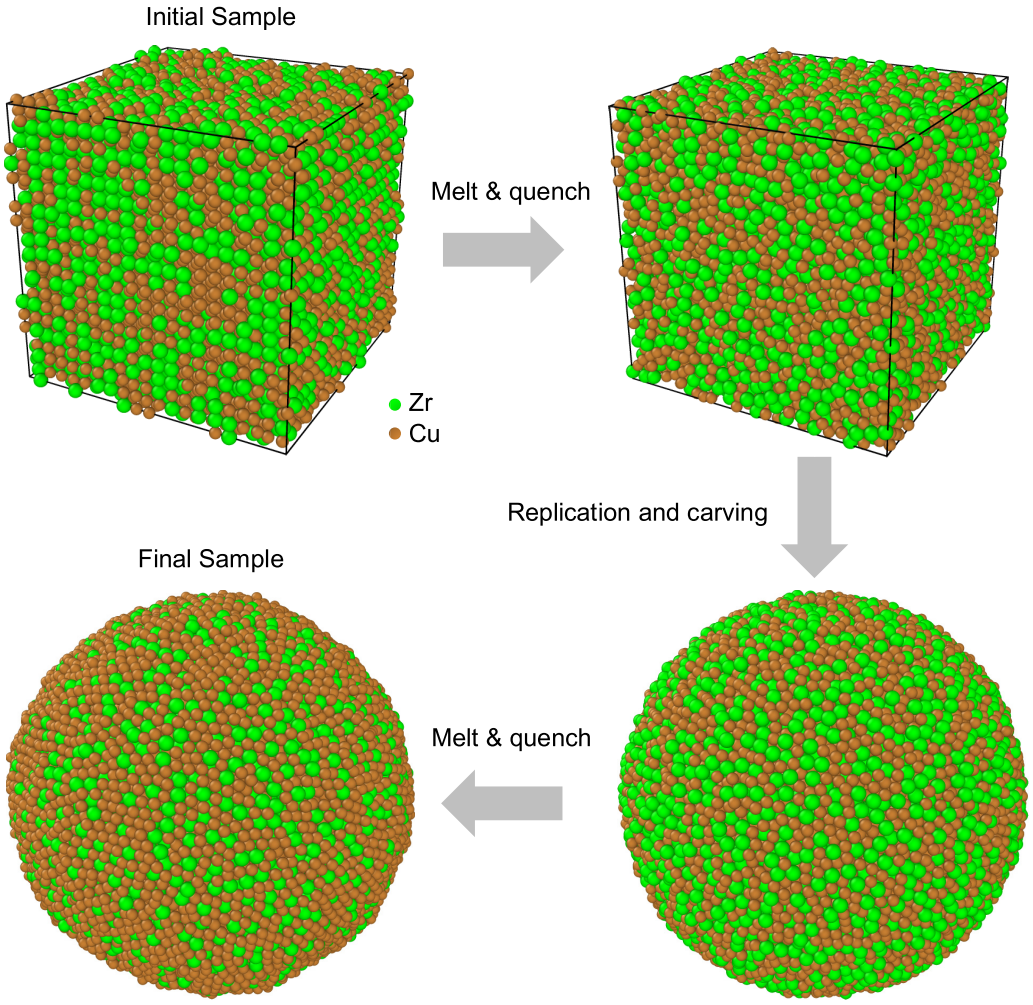

FIG. 1. Illustration of the synthesis process of a 12-nm nanoparticle (NP) using molecular dynamics simulations.

have a small fraction of the number of atoms of those shells close to the surface. In comparison to the observed surface composition gradient, the Cu concentration is much more stable in each 0.5-nm shell and no clear size-dependent trend is observed. However, it is noticed that the average Cu fraction at each shell, marked by the black squares, lies below the overall 0.64 Cu fraction. This depleted Cu concentration for the core region, sized 5 nm for 6–20-nm NPs, is further quantified to be 0.625, and can be rationalized by the exceedingly high Cu concentration at the surface. This result further quantifies the trend shown in Fig. 3, indicating that while the high Cu concentration at the surface drops and fluctuates towards the NP core, the Cu concentration in the core does not reach the overall 0.64 concentration of the alloy.

We further quantify the structure of the MG NPs by turning to atomic Voronoi analysis and the quantification of the concentration of Cu full icosahedral (FI) motifs. Cu FI is among the most important motifs to understand the mechanical behavior of CuZr MG alloys [24]. A high concentration of Cu FI is associated with a dense and strong structure [25]. The Voronoi analysis yields the Voronoi polyhedron with its corresponding indices and atomic volumes for every atom in the system. To examine the distribution of Cu FI in the NPs, we removed surface atoms from the analysis, as those have ill-defined atomic polyhedra with exceedingly high atomic volumes and the absence of Cu FI motifs. We remove atoms with atomic Voronoi volume larger than 30 $Å^3$, as those severely deviate from the average atomic volume of $\sim$18 $Å^3$ for Zr and $\sim$15 $Å^3$ for Cu atoms; next, we also eliminate atoms located within 0.5 nm from the NP surface, which are identified by the previously deleted atoms. Figure 5 shows the fractions of FI Cu atoms from the total Cu atoms as a function of NP size using the criterion described to remove surface atoms. The fraction of Cu FI atoms gradually drops with particle size, suggesting a denser core in smaller NPs [25]. While additional dissection could be performed onto the NPs, a cutoff radius of 0.5 nm is sufficient to obtain statistics on the bulk region of the NPs. That can be concluded because the Cu composition enters an oscillating region after $\sim$0.4 nm from the surface, as shown in Fig. 3. This inference is also supported by Fig. 6, which shows the atomic volume in the bulk of the NP, visualized by excluding the outermost atoms and their neighbor atoms within a cutoff radius of 0.5 nm. This core region displays a nearly homogeneous atomic volume distribution with fluctuations distributed randomly throughout the NP. While Fig. 5 shows a gradual drop in Cu FI fraction with NP size, the 7-nm NP displays a lower value than expected, a deviation also noted in Fig. 2. Further

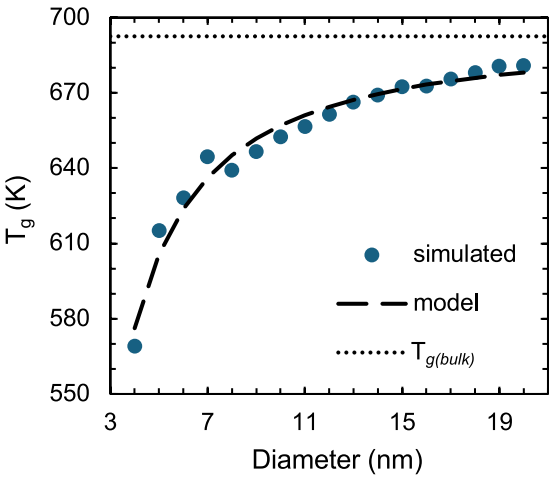

FIG. 2. Glass transition temperatures (T_g) for bulk MG (dotted line) and NPs with diameters ranging from 4 to 20 nm. The data points represent the simulated values, while the dashed line represents a model, derived considering the ratio of the surface area to the volume of the spherical-like NPs and the T_g of the bulk MG.

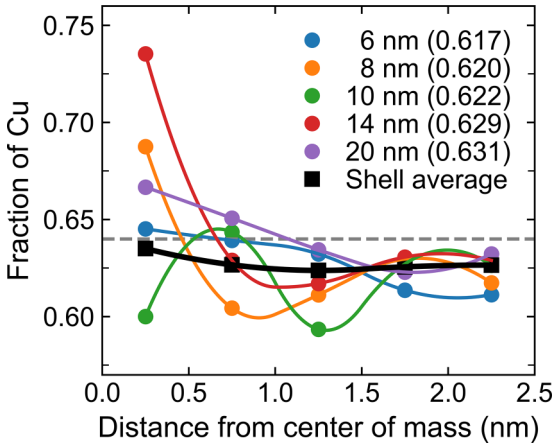

FIG. 4. Fraction of Cu in the core of NPs of 6, 8, 10, 14, and 20 nm. The plot displays the fraction of Cu in spherical shells of thickness 0.5 nm from the NP center of mass. A reference line, set at 0.64, represents the overall Cu fraction in the $Cu_{64}Zr_{36}$ NPs. The average Cu content for 6 – 20-nm samples within a cutoff radius of 2.5 nm is labeled in the legend.

examining, we calculate the density distribution function of distances to the center of mass for surface atoms (Fig. S2 [22]), which shows two peaks for the 7-nm NP. Arguably this is an indication that the shape of the 7-nm NP deviates from the spherical approximation (single peak) followed by all other NPs. This irregularity in shape might account for the observed discrepancy of results shown in Figs. 2 and 5.

To better understand the presence and distribution of Cu FI, it is worthwhile to discuss their formation during the quenching process. In Fig. 7 we show the evolution of the fraction of Cu FI during quenching as well as the formation and development of Cu FI clusters for the 12-nm-sized NP. The abrupt Cu FI network expansion is highlighted in Figs. 7(b)–7(f). At initial stages, when at temperatures of 1000 K and above, only isolated Cu FIs are observed within the NP, as shown in Fig. 7(b). However, as the temperature drops towards T_g (from the 12-nm NP quenching simulations we estimate T_g = 661 K), the number of Cu FIs increases sharply, generating a dense cluster network. Ultimately, the fraction of Cu FIs reaches a value of nearly 0.25 at low temperatures, with Cu FI clusters spanning a large volume of the NPs. An animation of the Cu FI network evolution is provided in the Supplemental Material [22].

Since the results demonstrate a strong effect of NP size on the observed T_g, calculated during quenching, we further investigate if the NP size influences other thermodynamic properties and behavior, such as the melting process. To study the melting process of the modeled NPs, we consider three heating rates: 10^{11}, 10^{12}, and 10^{13} K/s, as heating rates are known to strongly affect the melting process. Using the different heating rates, the potential energy as a function of system

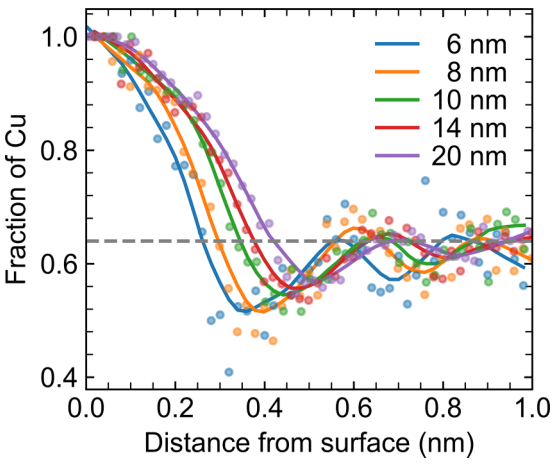

FIG. 3. Fraction of Cu atoms as a function of their distance from the surface of NPs with varying diameters of 6, 8, 10, 14, and 20 nm. The solid lines serve as a visual guide, and the dashed line indicates the value 0.64, which is the Cu fraction in the $Cu_{64}Zr_{36}$ system.

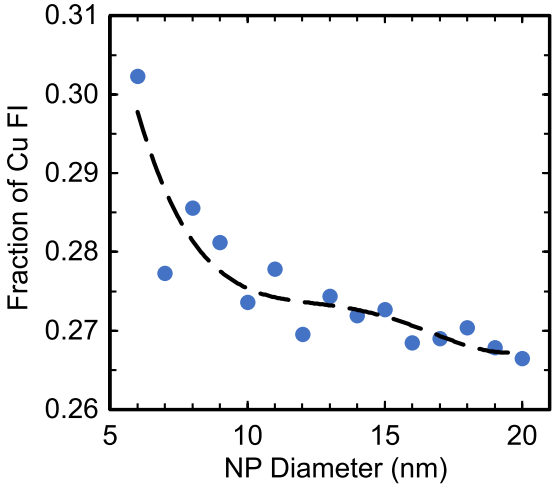

FIG. 5. Fraction of Cu atoms in the bulk of NPs with the Voronoi index of Cu⟨0, 0, 12, 0⟩, indicative of a full icosahedral (FI) structure, for 6-nm to 20-nm-sized NPs. The dashed line serves as a visual guide.

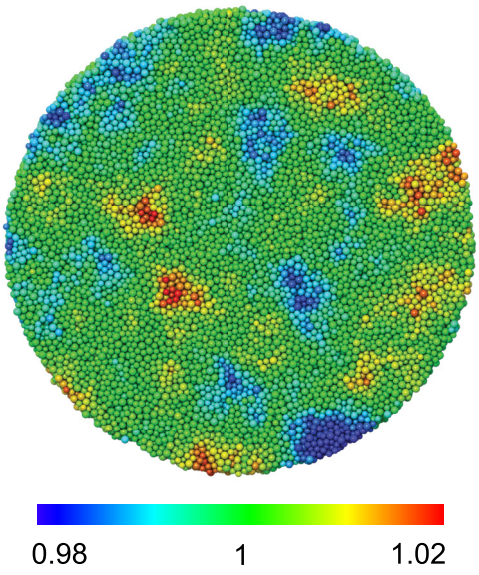

FIG. 6. Visualization of atomic volume distribution within a central slice cut of the 20-nm NP. The color scale represents relative atomic volumes, with the value of 1 indicating the mean atomic volume for all bulk atoms.

temperature is obtained, shown in Fig. 8 for the 20-nm-sized NPs. From the curves, we calculate the solidus and liquidus temperatures, which are identified as the initial points diverging from the linear interpolations calculated from points at low temperatures (pure solid) and high temperatures (pure liquid), as shown in Fig. 8(a). A threshold of 0.1% deviation is set as the criteria for the identification of both solidus and liquidus temperature values. Figure 9 shows the calculated solidus temperature as a function of NP size. Size effect appears at all heating rates even at the high rate of 10^{13} K/s for NPs in the 4–6-nm size range. Size effects become prominent for slower heating rates. For the rate 10^{12} K/s, the solidus temperature diminishes for smaller NPs in the 4–11-nm range. Meanwhile, at 10^{11} K/s, a prominent reduction in solidus temperature can be observed for NPs measuring 4–6 nm. One can note fluctuations in the solidus value for small NPs, i.e., NPs sized 4–6 nm, at all rates considered. Arguably, these are stochastic fluctuations that could possibly be minimized with the generation of multiple NPs at those sizes and the evaluation of an "average" value of the solidus temperature for the smallest NPs. Regardless, the fluctuation in the thermal properties of the smallest NPs does not change the clear size effects observed.

A detailed plot of both solidus and liquidus temperatures as a function of NP size and simulated heating rate is presented in Fig. 10. Each vertical line in Fig. 10 represents the temperature range for a specific NP diameter at a particular heating rate, indicating how the range varies with particle size and heating rate. The liquidus temperatures, marking the upper end of the temperature range, fluctuate for NPs ranging 4–12 nm, while the values for larger NPs remain constant. Overall, the data do not indicate a clear size dependence, yet the influence of the heating rate is evident. The temperature range between solidus and liquidus points is notably wider for the 10^{13} K/s heating rate compared to slower rates, as illustrated in Fig. 8(b). This phenomenon can be attributed to the overshooting effect resulting from rapid heating, where the system lacks sufficient simulation time to properly thermalize near the critical solidus and liquidus transition points.

IV. DISCUSSION

It is instructive to compare the results obtained here using melt quenching of spherical MG samples with those reported in the literature. The melt-and-quench procedure is preferred in MD simulations since it allows easier control of the size of the NPs. In general, the results obtained here with slow-quenched $Cu_{64}Zr_{36}$ NPs, i.e., using 10^9 K/s, show comparable properties to similar NPs produced at faster quenching rates, e.g., using $\sim 10^{10}$ K/s. According to Adajaoud *et al.* [18], the 7-nm $Cu_{64}Zr_{36}$ NP quenched at 10^{10} K/s has a shell region about 0.5 nm wide and a Cu fraction of 0.61 in the core region, which is similar to the characteristics of our 7-nm sample with a 0.3-nm-thick high Cu fraction layer and a Cu concentration of 0.615 in the central 5-nm core. Additionally, our compositional results capture a size-dependent trend on the surface segregation effect—i.e., larger NPs have a thicker Cu-rich layer. A previous study of the size-dependent properties of CuZr NPs by Zhang *et al.* [13] has considered NPs with sizes in the range 1.1–6.0 nm quenched at a high rate of 10^{12} K/s. They reported a size-dependent thermal behavior showing that a higher surface-to-volume ratio decreases T_g. Our results shown in Fig. 2 indicate that this trend is well defined and extends to large particles of up to 20 nm size. Similar to crystalline metallic NPs [23], the surface effect decreases for larger NPs and the value of T_g asymptotically points to the value at bulk, $T_{g(\text{bulk})}$.

An important application of well-relaxed MG NPs is in the fabrication of realistic nanoglass models [4,5,7,15,26,27]. Nanoglass models may be constructed directly using the mathematically defined regions of a Voronoi tessellated system. However, recent simulations have shown that only nanoglass models constructed from well-relaxed MG NPs can reproduce the high levels of excess free volume found in experiments [6]. Therefore, the deeply relaxed NP samples reported here will allow the synthesis of realistic nanoglass models. Besides, simulation reports have established an effect of grain sizes on the mechanical properties of nanoglasses [6,12,27]. Given this grain size is determined by the NPs employed, learning the structural properties, and having a library of NPs for establishing future studies, is essential. Hence, we expect the NP library constructed in the wide range of sizes from 1 to 20 nm to support future research on nanoglasses, including further studies of grain size effects [6,12,17,28–30], gradient in grain size [31,32], mechanical properties [12,16,32], and heterogeneous MG structures [33–35].

In evaluating the robustness of our simulation results, it is crucial to consider the potential impact of impurities, which may introduce significant deviations from the ideal condition in our study. The dramatic increase in the surface-to-volume ratio is likely to affect the chemical interactions between the surface and impurities. In contrast to bulk MGs (BMGs), MG NPs are commonly synthesized using magnetron sputtering in an inert gas condensation system [36] to limit oxidation and contamination. Nevertheless, MG NPs may develop surface

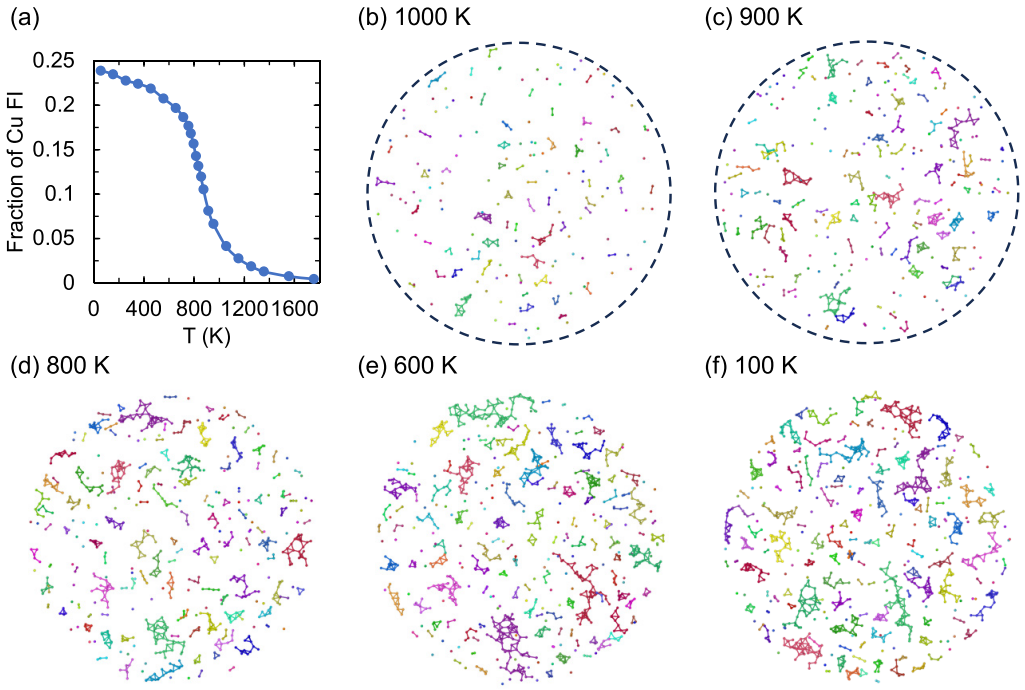

FIG. 7. Fraction and clustering of Cu FI in a 12-nm NP during quenching. (a) Plot showing the increasing fraction of Cu FI atoms with decreasing temperature. (b)–(f) Visualization of Cu FI atom clusters in a central 10 Å thick slice of the NP at temperatures of 1000 K, 900 K, 800 K, 600 K, and 100 K, respectively. Different colors indicate unique clusters, showcasing their evolution during the quenching process.

oxidation when they are exposed to oxygen. It is informative to draw parallels with experimental observations of oxidation kinetics in BMGs. Xu *et al.* documented a bilayer microstructure in oxidized amorphous $Cu_{33}Zr_{67}$ alloy, comprising an amorphous ZrO_2 overlayer and a Zr-depletion zone with Cu-enriched amorphous spherical inclusions [37]. This was attributed to the higher oxygen affinity of Zr than Cu in a Cu-Zr system [38]. By comparison, Zhang *et al.* reported the observation of multiple oxide layers in $Cu_{64}Zr_{36}$ MG powders, where the particle surface was covered by a Cu-enriched layer as a result of the outward ionic diffusion of Cu, followed by a Zr-enriched region [39]. Our results suggest that the composition distribution and amorphous structure of MG NPs, which vary significantly with NP size as shown in our study, could markedly influence the oxidation rate, phase composition, and thickness of the oxidation layer. The oxidation process resulting in the ZrO_2 layer may be prevented by the thicker Cu-coated surface layer of the larger NPs. This resonates with the finding of Zhang *et al.*, that a reduction in particle size significantly increases the oxidation rate [39]. Nonetheless, to fully elucidate the oxidation kinetics of MG NPs, it is crucial to extend research beyond particle size, incorporating factors such as surface morphology, microstructure, and diffusion time into the analysis.

It is worth mentioning that the simulations of the smallest NPs indicated a possible deficiency in the EAM potential

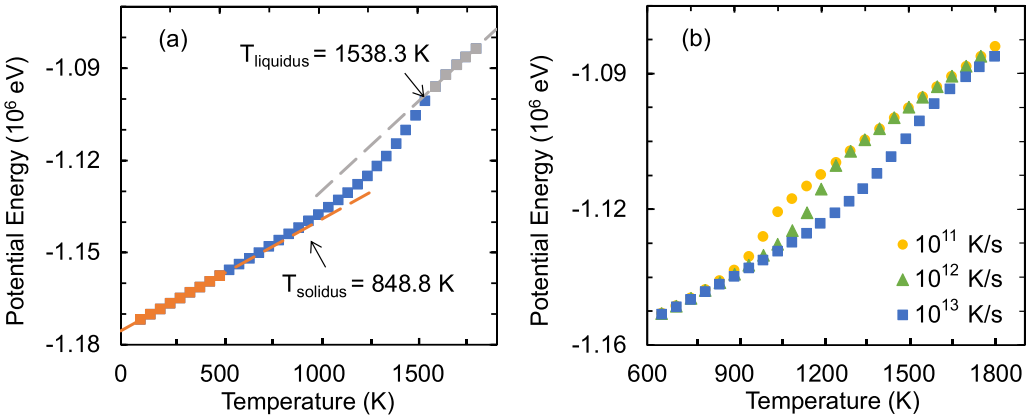

FIG. 8. Potential energy versus temperature for the 20-nm NP during heating. (a) Potential energy changes when the NP is heated at a rate of 10^{13} K/s. The orange and gray dashed curves are interpolations of low and high temperature points. (b) Comparison of energy changes for the NP heated at 10^{11}, 10^{12}, and 10^{13} K/s heating rates.

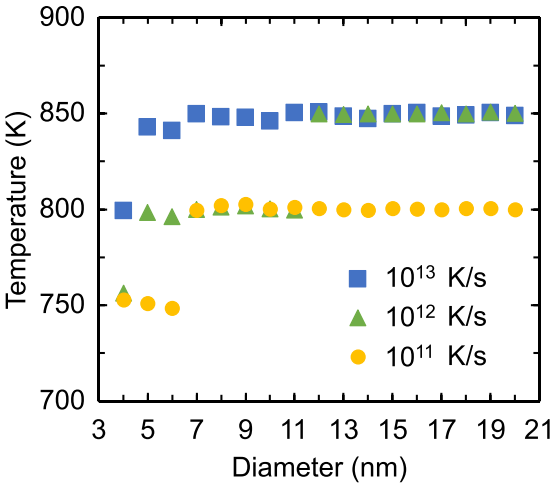

FIG. 9. Solidus temperatures for NPs of varying diameters from 4 nm to 20 nm under various heating rates. The data points are indicated by different markers: squares for 10^{13} K/s, triangles for 10^{12} K/s, and circles for 10^{11} K/s.

modeling of small MG clusters and NPs. In addition to results discussed for the 4–20-nm NPs, we also produce 1–3-nm-sized NPs. Nevertheless, upon examination of the formation of the NPs under quenching (Fig. S3 [22]), it becomes evident that NPs with sizes below 4 nm show abnormal energy evolutions. NPs sized 4 nm or larger display well-defined slopes in the liquid, supercooled liquid, and glass states, allowing precise calculations of T_g values, as shown in Fig. S1. In contrast, Fig. S3 indicates ill-defined slopes for the glass state, which can be larger or smaller than that of the liquid state

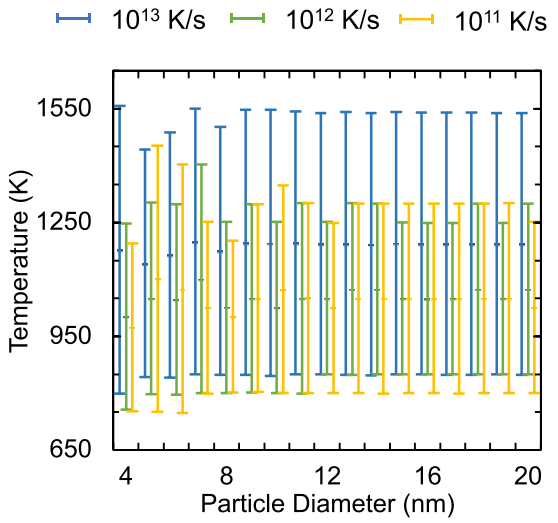

FIG. 10. Temperature interval between solidus and liquidus points for NPs with diameters ranging from 4 nm to 20 nm. The temperature ranges are shown at heating rates of 10^{13} K/s (blue), 10^{12} K/s (green), and 10^{11} K/s (orange).

(Figs. S3b and S3c). In addition, one can note discontinuity in the potential energy observed during the quenching process, which is a clear indication of a discontinuous interatomic potential. To further investigate this issue, we calculate the surface energy of the NPs, which is shown in Table I. The surface energies for all NPs are calculated by determining the potential energy difference between each NP at $T = 0$ K and a comparable bulk system with the same atom count. This energy difference is then divided by the estimated surface area of the NP, which is based on the sphere model using the nanoparticle diameter. Discrepancies for 1–3-nm NPs are also detected in the distinctive downward trend in surface energies for increasing NP size, whereas for the NPs in the 4–20-nm size range the trend is upward with minor fluctuations. Such positive correlation is expected on the basis of classical thermodynamics, as the number of next neighbors for surface atoms is reduced with decreasing particle size [40]. We speculate that the EAM potential model used here [20] may require revisions to accurately estimate the energy and describe the dynamics of very small NPs, i.e., with less than 3-nm diameter, where the local density can severely deviate from the bulk value. Because of the observed inconsistencies shown in Fig. S3, we chose to report and discuss only the results and analyses of NPs in the range 4–20 nm.

V. CONCLUSION

To extend the knowledge of glassy metals, this paper investigated $Cu_{64}Zr_{36}$ NPs sized 1–20 nm finely simulated at a comparatively slow quenching rate of 10^9 K/s. Using analytical tools, size-dependent properties are observed for the physical properties of NPs. A thicker Cu-coated surface layer, a lower Cu FI density thus a softer core, as well as higher glass transition, solidus, and liquid temperatures are perceived for larger NPs. These findings presented in this paper not only advance our understanding of MG NPs but also offer a road map for the development of MG composites that utilize glassy NPs, especially where size-dependent properties of MG NPs alter the performances of the products. With enhanced nanotechnology, the knowledge gained from this study will continue to be instrumental in shaping the future of materials science, leading to desirable innovations across various industries.

ACKNOWLEDGMENTS

The research was supported by the US Department of Energy, Office of Science, Office of Basic Energy Sciences, under Award No. DE-SC0020295. The work of S.Y. was performed under the auspices of the US Department of Energy, Lawrence Livermore National Laboratory, Contract No. DE-AC52-07NA27344. The authors acknowledge the Center for Advanced Research Computing (CARC) at the University of Southern California for providing computing resources that have contributed to the research results reported within this publication [41].

[1] J. Schroers, Processing of bulk metallic glass, Adv. Mater. **22**, 1566 (2010).

[2] M. M. Khan, A. Nemati, Z. U. Rahman, U. H. Shah, H. Asgar, and W. Haider, Recent advancements in bulk metallic glasses and their applications: A review, Crit. Rev. Solid State Mater. Sci. **43**, 233 (2018).

[3] Y. Ivanisenko, C. Kübel, S. H. Nandam, C. Wang, X. Mu, O. Adjaoud, K. Albe, and H. Hahn, Structure and properties of nanoglasses, Adv. Eng. Mater. **20**, 1800404 (2018).

[4] B. Cheng and J. R. Trelewicz, Interfacial plasticity governs strain delocalization in metallic nanoglasses, J. Mater. Res. **34**, 2325 (2019).

[5] H. Gleiter, T. Schimmel, and H. Hahn, Nanostructured solids–from nano-glasses to quantum transistors, Nano Today **9**, 17 (2014).

[6] K. Zheng, S. Yuan, H. Hahn, and P. S. Branicio, Excess free volume and structural properties of inert gas condensation synthesized nanoparticles based CuZr nanoglasses, Sci. Rep. **11**, 19246 (2021).

[7] C. Wang, D. Wang, X. Mu, S. Goel, T. Feng, Y. Ivanisenko, H. Hahn, and H. Gleiter, Surface segregation of primary glassy nanoparticles of $Fe_{90}Sc_{10}$ nanoglass, Mater. Lett. **181**, 248 (2016).

[8] V. V. Hoang and D. Ganguli, Amorphous nanoparticles—experiments and computer simulations, Phys. Rep. **518**, 81 (2012).

[9] Z. Song, W. Luo, X. Fan, and Y. Zhu, Atomic fast dynamic motion on the Cu nanoparticle's surface before melting: A molecular dynamics study, Appl. Surf. Sci. **606**, 154901 (2022).

[10] K. Zheng and P. S. Branicio, Synthesis of metallic glass nanoparticles by inert gas condensation, Phys. Rev. Mater. **4**, 076001 (2020).

[11] S. X. Liang, L. C. Zhang, S. Reichenberger, and S. Barcikowski, Design and perspective of amorphous metal nanoparticles from laser synthesis and processing, Phys. Chem. Chem. Phys. **23**, 11121 (2021).

[12] O. Adjaoud and K. Albe, Influence of microstructural features on the plastic deformation behavior of metallic nanoglasses, Acta Mater. **168**, 393 (2019).

[13] W. B. Zhang, J. Liu, S. H. Lu, H. Zhang, H. Wang, X. D. Wang, Q. P. Cao, D. X. Zhang, and J. Z. Jiang, Size effect on atomic structure in low-dimensional Cu-Zr amorphous systems, Sci. Rep. **7**, 7291 (2017).

[14] K. Albe, Y. Ritter, and D. Şopu, Enhancing the plasticity of metallic glasses: Shear band formation, nanocomposites and nanoglasses investigated by molecular dynamics simulations, Mech. Mater. **67**, 94 (2013).

[15] B. Cheng and J. R. Trelewicz, Controlling interface structure in nanoglasses produced through hydrostatic compression of amorphous nanoparticles, Phys. Rev. Mater. **3**, 035602 (2019).

[16] Y. Ritter, D. Sopu, H. Gleiter, and K. Albe, Structure, stability and mechanical properties of internal interfaces in $Cu_{64}Zr_{36}$ nanoglasses studied by MD simulations, Acta Mater. **59**, 6588 (2011).

[17] D. Şopu, K. Albe, Y. Ritter, and H. Gleiter, From nanoglasses to bulk massive glasses, Appl. Phys. Lett. **94**, 191911 (2009).

[18] O. Adjaoud and K. Albe, Interfaces and interphases in nanoglasses: Surface segregation effects and their implications on structural properties, Acta Mater. **113**, 284 (2016).

[19] A. P. Thompson *et al.*, LAMMPS - a flexible simulation tool for particle-based materials modeling at the atomic, meso, and continuum scales, Comput. Phys. Commun. **271**, 108171 (2022).

[20] M. I. Mendelev, Y. Sun, F. Zhang, C. Z. Wang, and K. M. Ho, Development of a semi-empirical potential suitable for molecular dynamics simulation of vitrification in Cu-Zr alloys, J. Chem. Phys. **151**, 214502 (2019).

[21] A. Stukowski, Visualization and analysis of atomistic simulation data with OVITO–the open visualization tool, Model. Simul. Mater. Sci. Eng. **18**, 015012 (2010).

[22] See Supplemental Material at http://link.aps.org/supplemental/10.1103/PhysRevMaterials.8.046001 for potential energy versus temperature for NP sizes 4–6 nm; probability density of deviation of surface atoms from average position for 5–10-nm NPs; potential energy versus temperature for NPs sized 1–3 nm; illustrations of the synthesized spherical-like NPs; and Cu FI growth evolution animation.

[23] G. Poletaev, Y. Bebikhov, and A. Semenov, Molecular dynamics study of the formation of the nanocrystalline structure in nickel nanoparticles during rapid cooling from the melt, Mater. Chem. Phys. **309**, 128358 (2023).

[24] Y. C. Yang, Z. Xia, and S. Mukherjee, Unraveling the structural statistics and its relationship with mechanical properties in metallic glasses, Nano Lett. **21**, 9108 (2021).

[25] Y. Q. Cheng, A. J. Cao, H. W. Sheng, and E. Ma, Local order influences initiation of plastic flow in metallic glass: Effects of alloy composition and sample cooling history, Acta Mater. **56**, 5263 (2008).

[26] S. H. Nandam, O. Adjaoud, R. Schwaiger, Y. Ivanisenko, M. R. Chellali, D. Wang, K. Albe, and H. Hahn, Influence of topological structure and chemical segregation on the thermal and mechanical properties of Pd–Si nanoglasses, Acta Mater. **193**, 252 (2020).

[27] M. M. Wang, M. T. Kiani, A. Parakh, Y. Jiang, and X. W. Gu, Effect of grain size on iron-boride nanoglasses, J. Mater. Sci. Technol. **141**, 116 (2023).

[28] D. Şopu and K. Albe, Influence of grain size and composition, topology and excess free volume on the deformation behavior of Cu–Zr nanoglasses, Beilstein J. Nanotechnol. **6**, 537 (2015).

[29] S. Adibi, P. S. Branicio, Y. W. Zhang, and S. P. Joshi, Composition and grain size effects on the structural and mechanical properties of CuZr nanoglasses, J. Appl. Phys. **116**, 043522 (2014).

[30] S. Adibi, P. S. Branicio, and S. P. Joshi, Suppression of shear banding and transition to necking and homogeneous flow in nanoglass nanopillars, Sci. Rep. **5**, 15611 (2015).

[31] S. Yuan and P. S. Branicio, Gradient microstructure induced shear band constraint, delocalization, and delayed failure in CuZr nanoglasses, Int. J. Plast. **134**, 102845 (2020).

[32] S. Yuan and P. S. Branicio, Atomistic simulations of nanoindentation on nanoglasses: Effects of grain size and gradient microstructure on the mechanical properties, Intermetallics **153**, 107782 (2023).

[33] Y. Lu, S. Su, S. Zhang, Y. Huang, Z. Qin, X. Lu, and W. Chen, Controllable additive manufacturing of gradient bulk metallic glass composite with high strength and tensile ductility, Acta Mater. **206**, 116632 (2021).

[34] N. Fan, C. Huang, Z. Wang, P. Yu, W. Chen, R. Lupoi, Q. Xie, L. Liu, and S. Yin, Interparticle bonding and interfacial

nanocrystallization mechanisms in additively manufactured bulk metallic glass fabricated by cold spray, Addit. Manuf. **58**, 103057 (2022).

[35] H. Ding *et al.*, Achieving strength-ductility synergy in metallic glasses via electric current-enhanced structural fluctuations, Int. J. Plast. **169**, 103711 (2023).

[36] S. H. Nandam *et al.*, Cu-Zr nanoglasses: Atomic structure, thermal stability and indentation properties, Acta Mater. **136**, 181 (2017).

[37] Y. Xu, L. P. H. Jeurgens, P. Schützendübe, S. Zhu, Y. Huang, Y. Liu, and Z. Wang, Effect of atomic structure on preferential oxidation of alloys: Amorphous versus crystalline Cu-Zr, J. Mater. Sci. Technol. **40**, 128 (2020).

[38] M. W. Chase, *NIST-JANAF Thermochemical Tables*, 4th ed. (American Institute of Physics, Gaithersburg, 1998).

[39] M. Zhang, Y. F. Ma, T. Huang, P. Gong, Y. Wang, H. J. Cai, Q. M. Li, X. Y. Wang, and L. Deng, High-temperature oxidation behavior of $Cu_{64}Zr_{36}$ metallic glass powders, Trans. Nonferrous Met. Soc. China **33**, 1814 (2023).

[40] D. Vollath, F. D. Fischer, and D. Holec, Surface energy of nanoparticles - influence of particle size and structure, Beilstein J. Nanotechnol. **9**, 2265 (2018).

[41] https://carc.usc.edu.